Large global scale vegetation sensitivity to daily rainfall variability

Andrew F. Feldman[1,2]*, Alexandra G. Konings[3], Pierre Gentine[4], Mitra Asadollahi[4], Lixin Wang[5], William K. Smith[6], Joel A. Biederman[7], Abhishek Chatterjee[8], Joanna Joiner[9], Benjamin Poulter[1]

[1]Biospheric Sciences Laboratory, NASA Goddard Space Flight Center, Greenbelt, MD, USA
[2]Earth System Science Interdisciplinary Center, University of Maryland, College Park, MD, USA
[3]Department of Earth System Science, Stanford University, Stanford, California, USA
[4]Department of Earth and Environmental Engineering, Columbia University, New York, New York, USA
[5]Department of Earth and Environmental Sciences, Indiana University Indianapolis, Indianapolis, Indiana, USA
[6]School of Natural Resources and the Environment, University of Arizona, Tucson, Arizona, USA
[7]Agricultural Research Service, U.S. Department of Agriculture, Tucson, Arizona, USA
[8]Jet Propulsion Laboratory, California Institute of Technology, Pasadena, CA, USA
[9]Atmospheric Chemistry and Dynamics Laboratory, NASA Goddard Space Flight Center, Greenbelt, MD, USA

*Corresponding Author: Andrew F. Feldman, andrew.feldman@nasa.gov

Rainfall events are globally becoming less frequent but more intense under a changing climate, thereby shifting climatic conditions for terrestrial vegetation independent of annual rainfall totals[1–3]. However, it remains uncertain how changes in daily rainfall variability are affecting global vegetation photosynthesis and growth[3–17]. Here, we use several satellite-based vegetation indices and field observations indicative of photosynthesis and growth, and find that global annual-scale vegetation indices are sensitive to the daily frequency and intensity of rainfall, independent of the total amount of rainfall per year. Specifically, we find that satellite-based vegetation indices are sensitive to daily rainfall variability across 42% of the vegetated land surfaces. On average, vegetation's sensitivity to daily rainfall variability is almost as large (95%) as vegetation's sensitivity to annual rainfall totals. Moreover, we find that wet day frequency and intensity are projected to change with similar magnitudes and spatial extents compared to annual rainfall changes. Overall, our findings suggest that daily rainfall variability and its trends are affecting global vegetation photosynthesis, with potential implications for the carbon cycle and food security.

Earth's vegetation regulates the global water and carbon cycles, thus strongly influencing weather and climate[18]. Climate change is altering both rainfall mean and variability, which influences vegetation function including plants' ability to provide food and take up atmospheric carbon dioxide[19–22]. Impacts of annual rainfall totals on vegetation have been extensively studied[19,23–25]. However, some studies have pointed out that annual rainfall totals only partially explain the interannual variability of photosynthesis, at times less than 50% even in water-limited ecosystems[26–28]. Furthermore, how plants respond to water availability in Earth system models is a dominant driver of global carbon cycle uncertainty[21,29,30], and thus changes in moisture might be having a greater impact on greening trends relative to CO_2 fertilization[31–33]. Potentially, there are overlooked aspects of rainfall's influence on annually averaged vegetation function that limit prediction of plant behavior and influence on the carbon cycle.

While trends in annual rainfall totals are heterogeneous and uncertain[34], a more robust trend in rainfall variability has emerged: daily rain events, or wet days, are becoming less frequent, but more intense[1–3] (Extended Data Figs. 1 and 2). As is evident from field experiments, plants are sensitive to this daily rainfall variability regardless of changes in annual rainfall totals[10]. More intense rainfall events generally increase infiltration and soil moisture[4,10,35]. Longer dry spells can also result in more plant stress from higher vapor pressure deficit and incoming surface solar radiation[11,36]. However, studies broadly conflict[3,12], with less frequent, more intense rain events causing positive[4], negative[13], or no response[14] in vegetation function (function refers here to photosynthesis and growth). Some studies indicate that these daily rainfall variability changes only marginally influence vegetation function[11,13,15,16]. Others show plant responses of up to 30%[5,17], which could have a substantial impact on the carbon cycle. Furthermore, most methods are limited in their ability to determine global plant responses to daily rainfall variability. Field manipulation experiments have limited spatial scale and extent[6]. Satellite-based studies tend to evaluate spatial rather than temporal relationships[7,8,11,13,16]. Process models were developed to evaluate seasonal dynamics and might struggle to capture sub-weekly wetting and drying cycles[37,38]. Ultimately, despite large impacts of mean moisture availability on plants[19,39], it is unclear how changes in daily-scale rainfall variability impact global vegetation and carbon budgets.

Here, we ask: to what degree is global vegetation function sensitive to climatic shifts in daily rainfall frequency and intensity, especially when compared to variations in annual rainfall totals? Is global vegetation function higher or lower in years with less frequent, more intense rainfall?

To address these questions, consensus is gained from four different satellite sources that are observational, have decade-long records, span global biomes, and vary in spectral range and resolution; two are normalized difference vegetation index (NDVI), and two are solar induced fluorescence (SIF) (Methods). We refer to satellite NDVI and SIF observations as vegetation indices for simplicity, acknowledging that their reflectance and emission properties are proxies, to varying degrees, of photosynthetic carbon uptake, greenness, vegetation cover, and biomass[40,41]. Furthermore, we evaluate multi-decadal globally observed and projected rainfall trends and estimate their influence on vegetation function.

Global vegetation sensitivity estimates

We use partial least square regressions to isolate the vegetation sensitivity to daily rainfall variability, while controlling for annual rainfall totals and several other climatic factors (including surface downwelling solar radiation, land surface temperature, and atmospheric humidity; see Methods). A challenge is that wet day frequency and intensity are inherently related to annual rainfall totals[42]. However, our tests reveal that wet day frequency (or wet day intensity) and annual rainfall total have enough uncorrelated variability that they can be statistically partitioned within our regressions (Methods; Extended Data Fig. 3). For our main analysis, we use wet day frequency alone to represent less frequent, more intense wet days. Specifically, by including both wet day frequency and annual rainfall total as regressors, a decrease in wet day frequency (longer dry spells) also represents greater wet day intensity because annual rainfall totals are simultaneously controlled for. Wet day frequency and other metrics used here thus broadly represent daily rainfall variability. Additionally, note that these daily rainfall variability metrics are lumped parameters in capturing the daily rainfall itself, but also post-rain drying factors that include sub-seasonal variability of solar radiation and humidity (See Methods; Figs. S1, S2).

We find that global vegetation sensitivities to daily rainfall variability are similar in magnitude as the sensitivity to annual rainfall total (Fig. 1). Namely, a one standard deviation shift in daily rainfall variability (via wet day frequency or intensity) is related to between 20% to 50% changes in annual mean vegetation indices across a range of climatic conditions, similarly to annual rainfall total (Figs. 1a, 1b, S3). Consequently, daily rainfall variability explains 5-20% of the variance of mean vegetation indices, similarly to annual rainfall total (Fig. S4). In directly comparing their sensitivity magnitudes, the annual mean vegetation index sensitivity magnitude to daily rainfall variability is a factor of 0.95 (0.61-1.46, hereafter the range refers to 25th and 75th percentile bounds across space) of the magnitude of the vegetation sensitivity to annual rainfall total, based on our partial regression approach (Fig. 1c). Similar conclusions are drawn when using different daily rainfall variability metrics, using soil moisture variability instead of rainfall data, considering only the growing season, and when using a random forest regression approach (Fig. 1c). The ratio is even higher at 1.58 (1.08-2.28) when analyzing ground measurements, although this field network analysis relies on binning multiple sites and is thus more uncertain (see Methods).

Additionally, vegetation sensitivity to daily rainfall variability is significant ($p<0.05$) across 42% of Earth's vegetated land surfaces (Fig. 1a). For comparison, this spatial extent is 50% when considering vegetation sensitivity to annual rainfall totals (Fig. 1b). While there is some variability of the fractional area with significant sensitivities when repeating analyses across different wet day metrics and satellite datasets, it is always comparable to the fractional area with significant sensitivities to annual rainfall totals (Figs. S5, S6).

An example of the vegetation sensitivity to daily rainfall variability is shown in dry savannas in Botswana (Fig. 2). There, NDVI was larger by 16% in a year that had more intense, less frequent rainfall events compared to another year, despite both years having nearly identical annual rainfall totals.

Previous investigations have found that plant sensitivity to sub-seasonal rainfall variability is only a small fraction, often less than 20%, of the plant sensitivity to annual rainfall totals[9,11,13,16]. We instead find that plant sensitivity to changes in wet day frequency and intensity are 95% (61%-146%) as large as their sensitivity to annual rainfall totals (Fig. 1c), several times higher than previous estimates (Fig. 1c). We attribute these differences in part to our analysis relying directly on temporal patterns with decade long records of observed vegetation variables, rather than on mainly spatial relationships in previous studies[13,16]. Furthermore, despite some differences in results across datasets and approaches (see text in SI), we emphasize our findings about the sensitivity magnitudes and spatial extents are robust across many conditions (Figs. S5-S12).

Potential drivers of spatial patterns

We evaluate vegetation sensitivities to less frequent, more intense wet days along a gradient of mean annual rainfall in order to provide a first-order understanding of differences in vegetation function between shorter, herbaceous plants that receive less annual rainfall and taller, woody plants that receive more annual rainfall. We find that in arid ecosystems, vegetation indices are higher in years with less frequent, more intense wet days, while in humid ecosystems, vegetation indices are typically lower in such years (Fig. 3a). Specifically, for dry ecosystems receiving less than 500 mm of annual rainfall, 23% of pixels show increased vegetation indices while 13% show decreases in years with less frequent, more intense wet days. By contrast, for humid ecosystems receiving more than 1,500 mm of annual rainfall, 22% of pixels show vegetation index increases while 31% show decreases in years with less frequent, more intense wet days. These patterns of changing signs of responses between dry and wet ecosystems are captured across most datasets and conditions (Fig. S13), though with some differences (see SI). They are also consistent with a previously posed theoretical paradigm and with results from field experiments[3,6,43].

Grasslands and shrublands, prevalent in drier regions, as well as croplands tend to experience increased vegetation indices in years with less frequent, more intense wet days (Fig. 3b). Boreal needleleaf forests occupying higher latitudes (Fig. S14) also show increased vegetation indices under these conditions, potentially due to increases in light availability over longer dry periods. Savannas which typically occupy transitional regions, tend to show both positive and negative vegetation sensitivities (Fig. 3b). Humid forests that occupy lower and mid-latitudes (Fig. S14; broadleaf forests) tend to have an opposing relation of lower vegetation indices in years with less frequent, more intense wet days (Fig. 2b). This decreasing vegetation index signal mainly comes from forests in the Indo-Pacific Islands (Fig. 1a) that might respond negatively to longer dry spells. In contrast, some portions of the Amazon and Congo rainforests have a positive response (Fig. 1a), likely because more light and higher vapor pressure deficit (VPD) benefit these ecosystems[44].

To gain further insights into diverging signs of plant responses, we use a regression and variance decomposition method to evaluate the degree to which several soil, plant, and atmospheric variables explain the spatial pattern of vegetation sensitivities to less frequent, more intense wet days (Methods). Several main explanatory variables arise (Extended Data Fig. 4; $p<0.05$). Specifically, drier ecosystems tend to have increased vegetation indices in years with less frequent, more intense wet days because these ecosystems spend more time below plant water stress thresholds and thus larger rainfall events are more ecologically advantageous by increasing soil moisture above these thresholds. Drier ecosystems also have greater plant response sensitivities to individual wet days, such that larger rain events can greatly increase plant function[37,45,46] (Fig. S15). Finally, these ecosystems have smaller mean VPD increases with less frequent, more intense wet days (Fig. S15), meaning they will experience relatively less plant water stress during dry spells. We tested several other factors, such as mean annual soil moisture sensitivity to more intense, less frequent rainfall events, but they were not found to be significant drivers of global vegetation sensitivity patterns (Fig. S15).

Daily rainfall variability trends

Finally, we estimate the daily rainfall frequency and intensity trends over historical periods from merged observation-based datasets (1980-2020), extrapolated in-situ observations (1950-2016), and models (1940-2020) as well as model projections between 2020-2099 (Methods). Common features across all datasets and time periods are that wet day frequency and intensity trends are nearly as high in relative magnitude and of similar spatial prevalence as trends in annual rainfall totals (Fig. 4a). For example, based on CMIP6 projections from 27 models, wet day frequency and intensity are changing by 0.7% and 1.2% per decade, respectively (Fig. 4a), while annual rainfall total is changing by 1.2% per decade. The areal coverage of significant ($p<0.05$) CMIP6 projected wet day frequency and intensity trends are 33% and 47% of global vegetated surfaces, respectively, which are similar to the 36% coverage for trends in annual rainfall totals. Trends over the historical period (pre-2020) are ultimately less spatially extensive; note that the areal percentages of significant trends have been reduced by 3-5 times after conservative removal of false positive trends (see methods, Fig. S16). However, we emphasize that our focus is on the comparison between daily rainfall variability trends and annual rainfall total trends for a given dataset; the feature that daily rainfall variability trend extent and magnitude is similar to that of trends in annual rainfall totals holds across observations (CPC and REGEN), model reanalysis (MERRA2), and model simulations over a longer record (CMIP6 historical model scenarios) (Fig. 4a). Our findings thus hold across different precipitation products ranging from the past to the future, showing robustness of our arguments even considering the limitations of each dataset (see SI).

Consequently, the presence of daily rainfall variability trends, together with widespread vegetation sensitivities to daily rainfall variability (Fig. 1), suggest an influence of daily rainfall variability trends on global vegetation photosynthesis and growth. We empirically estimate the impact of trends in daily rainfall variability on global vegetation indices (Fig. 4b; Methods). While the magnitudes of empirically estimated vegetation trends themselves are uncertain (see SI), a feature that emerges from estimates from each rainfall dataset is that estimated vegetation index trend magnitudes due to daily rainfall variability are similar to those due to trends in annual rainfall totals (Fig. 4b). For example, based on CMIP6 projections between 2020-2099, vegetation index trends due to both daily rainfall variability and annual rainfall totals are both 0.1%/decade.

The absolute trend magnitudes of vegetation indices due to changes in daily rainfall variability are |0.5%|/decade (|1.1%|/decade at 75th percentile) and |0.1%|/decade (|0.3%|/decade at 75th percentile) based on CPC and CMIP6 trends, respectively (Fig. 4b). For comparison, mean global vegetation greening is estimated to be 1% to 3% per decade since 1980, where CO_2 fertilization is expected to be playing a dominant role, with climate only driving a fraction of these changes[31]. Therefore, daily rainfall variability might be a dominant climate-based driver of global vegetation function changes.

Mean vegetation trends across the globe are ultimately near zero (Extended Data Fig. 5), attributable to averaging opposing vegetation sensitivities to less frequent, more intense wet days across dry to wet ecosystems (Figs. 1 and 2). As such, the global mean trend obscures large regional trends with estimated high magnitude vegetation trends present in the Western US, Australia, and Southern Africa (Extended Data Fig. 5), where presumably disparate and pronounced rainfall trends are occurring because of regional changes in atmospheric patterns[1], for example, the North American Monsoon and Walker Cell.

Discussion

In summary, we find robust, substantial, and globally widespread vegetation index sensitivities to how rainfall is delivered to the surface in terms of daily frequency and intensity, independent of total rainfall amounts. While the analysis is limited by statistical means to partition the relative plant sensitivities to daily rainfall variability, our uncertainty tests reveal robustness of our findings across a multitude of statistical approaches and across satellite and field datasets. Mean annual water availability has long been recognized as a major driver of vegetation function[25,47], but we argue that daily rainfall variability is playing a similarly large role on vegetation function at annual scales across the globe. Since annual rainfall totals strongly drive interannual variability of global photosynthesis and the carbon cycle, daily rainfall variability is likely also a substantial driver of this variability[48,49]. Our results also imply that aggregating vegetation observations to monthly, seasonal, or annual timescales for many types of analyses would miss essential response variability. Furthermore, while we do not explicitly investigate the role of the most extreme wet days or longest dry spells here, this study is consistent with and broadens the existing hypothesis that the most extreme wet days and lengthening dry spells are increasing in intensity and having a substantial role on the carbon cycle[50–52].

We also find that trends in wet day frequency and intensity are nearly as large and as spatially prevalent as trends in annual rainfall totals. With both daily rainfall variability trends and strong vegetation sensitivity to this variability, there are likely globally prevalent vegetation function trends due to less frequent, more intense wet days that are playing a role in global greening and browning[31,53,54]. Vegetation trend attribution analyses do not typically consider impacts of daily rainfall variability, and will thus miss these plant responses[1]. Therefore, changes in daily rainfall variability need to be explicitly considered when projecting terrestrial carbon uptake and managing agricultural and natural ecosystems.

References

1. Pendergrass, A. G., Knutti, R., Lehner, F., Deser, C. & Sanderson, B. M. Precipitation variability increases in a warmer climate. *Sci. Rep.* **7**, 1–9 (2017).
2. Pendergrass, A. G. & Knutti, R. The Uneven Nature of Daily Precipitation and Its Change. *Geophys. Res. Lett.* **45**, 11,980-11,988 (2018).
3. Feldman, A. F. *et al.* Plant responses to changing rainfall frequency and intensity. *Nat. Rev. Earth Environ.* (2024). doi:10.1038/s43017-024-00534-0
4. Thomey, M. L. *et al.* Effect of precipitation variability on net primary production and soil respiration in a Chihuahuan Desert grassland. *Glob. Chang. Biol.* **17**, 1505–1515 (2011).
5. Fay, P. A. *et al.* Relative effects of precipitation variability and warming on tallgrass prairie ecosystem function. *Biogeosciences* **8**, 3053–3068 (2011).
6. Liu, J. *et al.* Impact of temporal precipitation variability on ecosystem productivity. *Wiley Interdiscip. Rev. Water* **7**, e1481 (2020).
7. Sloat, L. L. *et al.* Increasing importance of precipitation variability on global livestock grazing lands. *Nat. Clim. Chang.* **8**, 214–218 (2018).
8. Ritter, F., Berkelhammer, M. & Garcia-Eidell, C. Distinct response of gross primary productivity in five terrestrial biomes to precipitation variability. *Commun. Earth&Environment* **1**, 34 (2020).
9. Guan, K. *et al.* Continental-scale impacts of intra-seasonal rainfall variability on simulated ecosystem responses in Africa. *Biogeosciences* **11**, 6939–6954 (2014).
10. Knapp, A. K. *et al.* Rainfall variability, carbon cycling, and plant species diversity in a mesic grassland. *Science (80-.).* **298**, 2202–2205 (2002).
11. Ross, I. *et al.* How do variations in the temporal distribution of rainfall events affect ecosystem fluxes in seasonally water-limited Northern Hemisphere shrublands and forests? *Biogeosciences* **9**, 1007–1024 (2012).
12. Su, J., Zhang, Y. & Xu, F. Divergent responses of grassland productivity and plant diversity to intra- annual precipitation variability across climate regions : A global synthesis. *J. Ecol.* **111**, 1–14 (2023).
13. Good, S. P. & Caylor, K. K. Climatological determinants of woody cover in Africa. *Proc. Natl. Acad. Sci. U. S. A.* **108**, 4902–4907 (2011).
14. Zhang, F. *et al.* Precipitation temporal repackaging into fewer, larger storms delayed seasonal timing of peak photosynthesis in a semi-arid grassland. *Funct. Ecol.* **36**, 646–658 (2021).
15. Xu, X., Medvigy, D. & Rodriguez-Iturbe, I. Relation between rainfall intensity and savanna tree abundance explained by water use strategies. *Proc. Natl. Acad. Sci.* **112**, 12992–12996 (2015).
16. Case, M. F. & Staver, A. C. Soil texture mediates tree responses to rainfall intensity in African savannas. *New Phytol.* **219**, 1363–1372 (2018).
17. Heisler-White, J. L., Blair, J. M., Kelly, E. F., Harmoney, K. & Knapp, A. K. Contingent productivity responses to more extreme rainfall regimes across a grassland biome. *Glob. Chang. Biol.* **15**, 2894–2904 (2009).
18. Jasechko, S. *et al.* Terrestrial water fluxes dominated by transpiration. *Nature* **496**, 347–350 (2013).
19. Green, J. K. *et al.* Large influence of soil moisture on long-term terrestrial carbon

uptake. *Nature* **565**, 476–479 (2019).
20. Rigden, A. J., Mueller, N. D., Holbrook, N. M., Pillai, N. & Huybers, P. Combined influence of soil moisture and atmospheric evaporative demand is important for accurately predicting US maize yields. *Nat. Food* **1**, 127–133 (2020).
21. Wang, L. *et al.* Dryland productivity under a changing climate. *Nature Climate Change* **12**, 981–994 (2022).
22. Isbell, F. *et al.* High plant diversity is needed to maintain ecosystem services. *Nature* **477**, 199–202 (2011).
23. Gherardi, L. A. & Sala, O. E. Effect of interannual precipitation variability on dryland productivity: A global synthesis. *Glob. Chang. Biol.* **25**, 269–276 (2019).
24. Nemani, R. R. *et al.* Climate-driven increases in global terrestrial net primary production from 1982 to 1999. *Science (80-.).* **300**, 1560–1563 (2003).
25. Maurer, G. E., Hallmark, A. J., Brown, R. F., Sala, O. E. & Collins, S. L. Sensitivity of primary production to precipitation across the United States. *Ecol. Lett.* **23**, 527–536 (2020).
26. Sala, O. E., Parton, W. J., Joyce, L. A. & Lauenroth, W. K. Primary Production of the Central Grassland Region of the United States. *Ecology* **69**, 40–45 (1988).
27. Biederman, J. A. *et al.* CO2 exchange and evapotranspiration across dryland ecosystems of southwestern North America. *Glob. Chang. Biol.* **23**, 4204–4221 (2017).
28. Ukkola, A. M. *et al.* Annual precipitation explains variability in dryland vegetation greenness globally but not locally. *Glob. Chang. Biol.* **27**, 4367–4380 (2021).
29. Trugman, A. T., Medvigy, D., Mankin, J. S. & Anderegg, W. R. L. Soil Moisture Stress as a Major Driver of Carbon Cycle Uncertainty. *Geophys. Res. Lett.* **45**, 6495–6503 (2018).
30. Denissen, J. M. C. *et al.* Widespread shift from ecosystem energy to water limitation with climate change. *Nat. Clim. Chang.* **12**, 677–684 (2022).
31. Zhu, Z. *et al.* Greening of the Earth and its drivers. *Nat. Clim. Chang.* **6**, 791–795 (2016).
32. Li, F. *et al.* Global water use efficiency saturation due to increased vapor pressure deficit. *Science (80-.).* **381**, 672–677 (2023).
33. Smith, W. K. *et al.* Large divergence of satellite and Earth system model estimates of global terrestrial CO2 fertilization. *Nat. Clim. Chang.* **6**, 306–310 (2016).
34. Trenberth, K. E. Changes in precipitation with climate change. *Clim. Res.* **47**, 123–138 (2011).
35. Lian, X., Zhao, W. & Gentine, P. Recent global decline in rainfall interception loss due to altered rainfall regimes. *Nat. Commun.* **13**, 7642 (2022).
36. Feldman, A. F., Short Gianotti, D. J., Trigo, I. F., Salvucci, G. D. & Entekhabi, D. Land-atmosphere drivers of landscape-scale plant water content loss. *Geophys. Res. Lett.* **47**, e2020GL090331 (2020).
37. Feldman, A. F. *et al.* Moisture pulse-reserve in the soil-plant continuum observed across biomes. *Nat. Plants* **4**, 1026–1033 (2018).
38. Williams, C. A., Hanan, N., Scholes, R. J. & Kutsch, W. Complexity in water and carbon dioxide fluxes following rain pulses in an African savanna. *Oecologia* **161**, 469–480 (2009).

39. Humphrey, V. *et al.* Sensitivity of atmospheric CO2 growth rate to observed changes in terrestrial water storage. *Nature* **560**, 628–631 (2018).
40. Sun, Y. *et al.* From remotely sensed solar-induced chlorophyll fluorescence to ecosystem structure, function, and service: Part I—Harnessing theory. *Glob. Chang. Biol.* **29**, 2926–2952 (2023).
41. Smith, W. K., Fox, A. M., MacBean, N., Moore, D. J. P. & Parazoo, N. C. Constraining estimates of terrestrial carbon uptake: new opportunities using long-term satellite observations and data assimilation. *New Phytol.* **225**, 105–112 (2020).
42. Fatichi, S., Ivanov, V. Y. & Caporali, E. Investigating interannual variability of precipitation at the global scale: Is there a connection with seasonality? *J. Clim.* **25**, 5512–5523 (2012).
43. Knapp, A. K. *et al.* Consequences of More Extreme Precipitation Regimes for Terrestrial Ecosystems. *Bioscience* **58**, 811–821 (2008).
44. Green, J. K., Berry, J., Ciais, P., Zhang, Y. & Gentine, P. Amazon rainforest photosynthesis increases in response to atmospheric dryness. *Sci. Adv.* **6**, 1–10 (2020).
45. Post, A. K. & Knapp, A. K. Plant growth and aboveground production respond differently to late-season deluges in a semi-arid grassland. *Oecologia* **191**, 673–683 (2019).
46. Feldman, A. F., Chulakadabba, A., Short Gianotti, D. J. & Entekhabi, D. Landscape-Scale Plant Water Content and Carbon Flux Behavior Following Moisture Pulses: From Dryland to Mesic Environments. *Water Resour. Res.* **57**, e2020WR027592 (2021).
47. Huxman, T. E. *et al.* Convergence across biomes to a common rain-use efficiency. *Nature* **429**, 651–654 (2004).
48. Poulter, B. *et al.* Contribution of semi-arid ecosystems to interannual variability of the global carbon cycle. *Nature* **509**, 600–603 (2014).
49. Ahlström, A. *et al.* The dominant role of semi-arid ecosystems in the trend and variability of the land CO2 sink. *Science (80-.).* **348**, 895–900 (2015).
50. Pendergrass, A. G. What precipitation is extreme? *Science (80-.).* **360**, 1072–1073 (2018).
51. Kannenberg, S. A., Bowling, D. R. & Anderegg, W. R. L. Hot moments in ecosystem fluxes: High GPP anomalies exert outsized influence on the carbon cycle and are differentially driven by moisture availability across biomes. *Environ. Res. Lett.* **15**, 054004 (2020).
52. Wainwright, C. M., Allan, R. P. & Black, E. Consistent Trends in Dry Spell Length in Recent Observations and Future Projections. *Geophys. Res. Lett.* **49**, (2022).
53. Piao, S. *et al.* Characteristics, drivers and feedbacks of global greening. *Nat. Rev. Earth Environ.* **1**, 14–27 (2020).
54. Higgins, S. I., Conradi, T. & Muhoko, E. Shifts in vegetation activity of terrestrial ecosystems attributable to climate trends. *Nat. Geosci.* **16**, 147–153 (2023).

Figure Legends

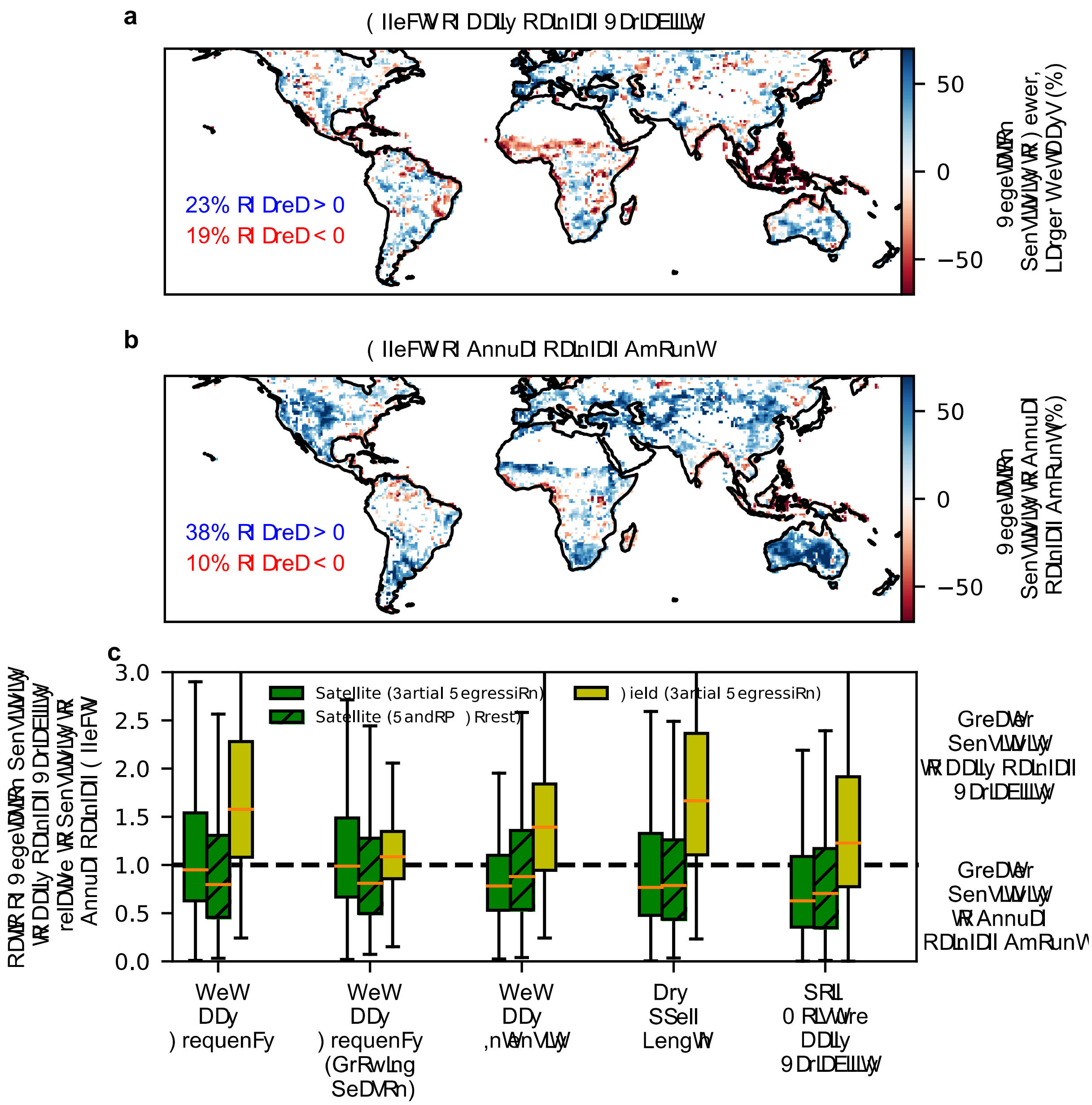

Fig. 1. | Sensitivity of vegetation function to daily rainfall variability is nearly as substantial and spatially extensive as its sensitivity to annual rainfall totals across much of the globe. (a) Satellite vegetation index sensitivity to less frequent, more intense wet days (represented by a one standard deviation decrease of wet day frequency; see Methods) based on a partial regression. Results are an ensemble mean of normalized sensitivities across MODIS NDVI, AVHRR NDVI, OCO-2 SIF, and GOME-2 SIF (Figs. S3, S5). Only significant values across all satellite datasets are shown (Methods). Percent areas refer to statistically significant sensitivities considering only vegetated pixels ($p<0.05$). High latitudes (>60 degrees) are not included in the

analysis (Methods). (b) Same as (a), but vegetation index sensitivities to a one standard deviation increase in annual rainfall total. (c) Ratio of vegetation sensitivity to less frequent, more intense wet days relative to sensitivity to annual rainfall totals. Boxplots are global spatial distributions. A random forest method applied to the satellite data and in-situ results from FLUXNET gross primary production are shown for comparison (Methods). Reported results are based on z-score annual anomalies of each dataset. The satellite data are available between 2003-2022, with 8 to 20 year date ranges, while the FLUXNET data include 178 sites with primarily data available between 1999-2014 with a median of 7 year date ranges (Table S1). Data from these tower sites are processed similarly to the satellite data (Methods).

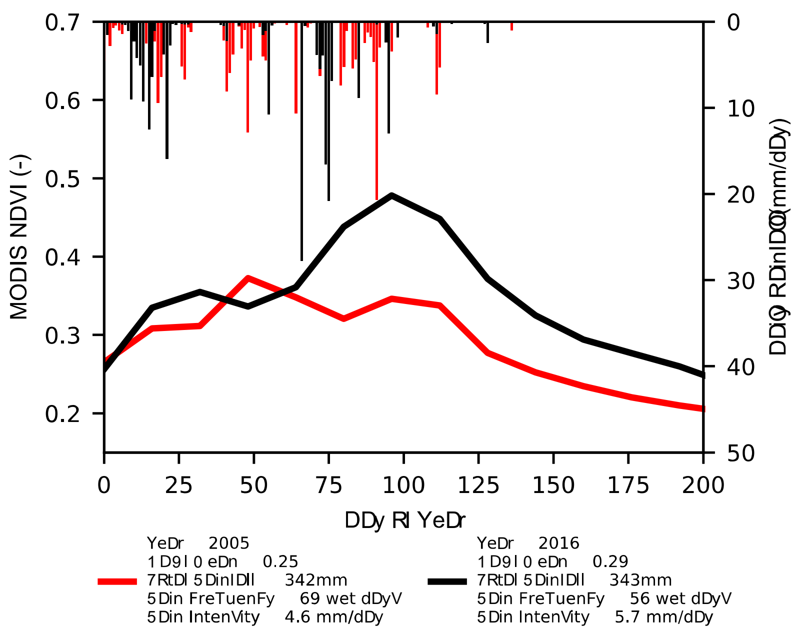

Fig. 2. | Example time series of dry savanna in Botswana (23°S, 22°E) where vegetation indices tend to be higher in years with more intense, less frequent rainfall events (based on results in Fig. 1). Comparison of vegetation indices between 2005 and 2016 which had nearly identical annual rainfall totals, but fewer wet days and larger mean rainfall events in 2016.

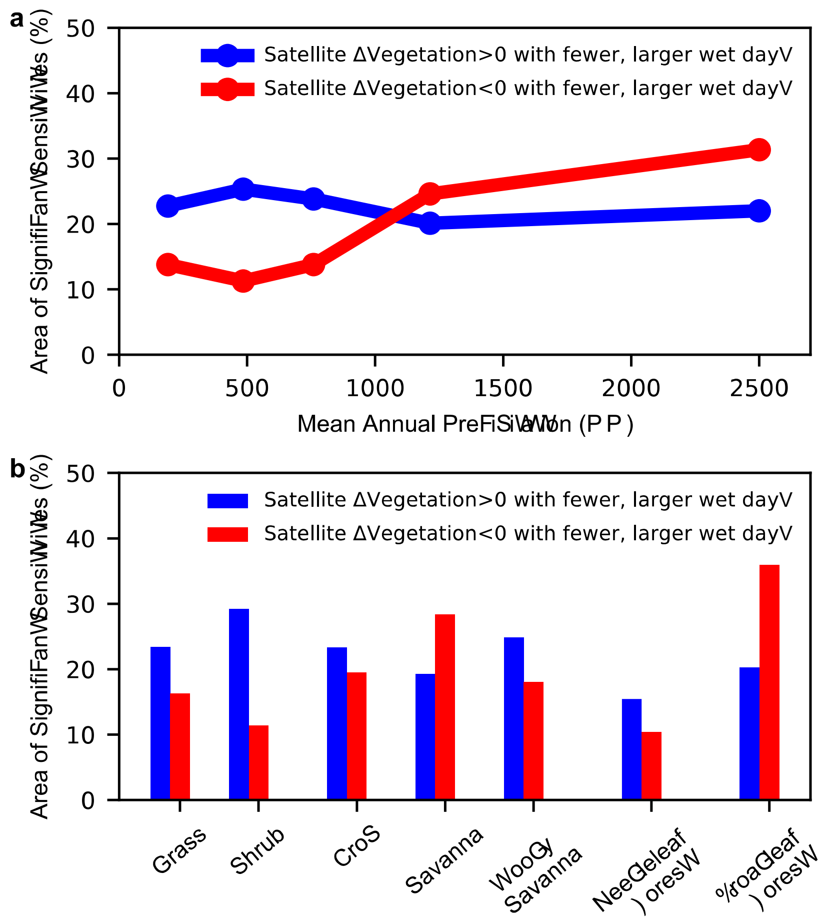

Fig. 3. | Vegetation indices in years with less frequent, more intense wet days tend to increase in drier ecosystems and decrease in wetter ecosystems. (a) Mean annual rainfall gradient of sign of vegetation sensitivity to less frequent, more intense wet days based on ensemble average across vegetation metrics from MODIS NDVI, AVHRR NDVI, OCO-2 SIF, and GOME-2 SIF (Fig. S13). Significance is determined across all four satellite-based vegetation indices (Methods). Rainfall bins have nearly equal sample sizes. These relationships are reproduced using alternative regression model selection techniques and daily rainfall variability regressors (Fig. S13). (b) Same as (a) but conditioning on different vegetation types using IGBP land cover classifications (Fig. S14).

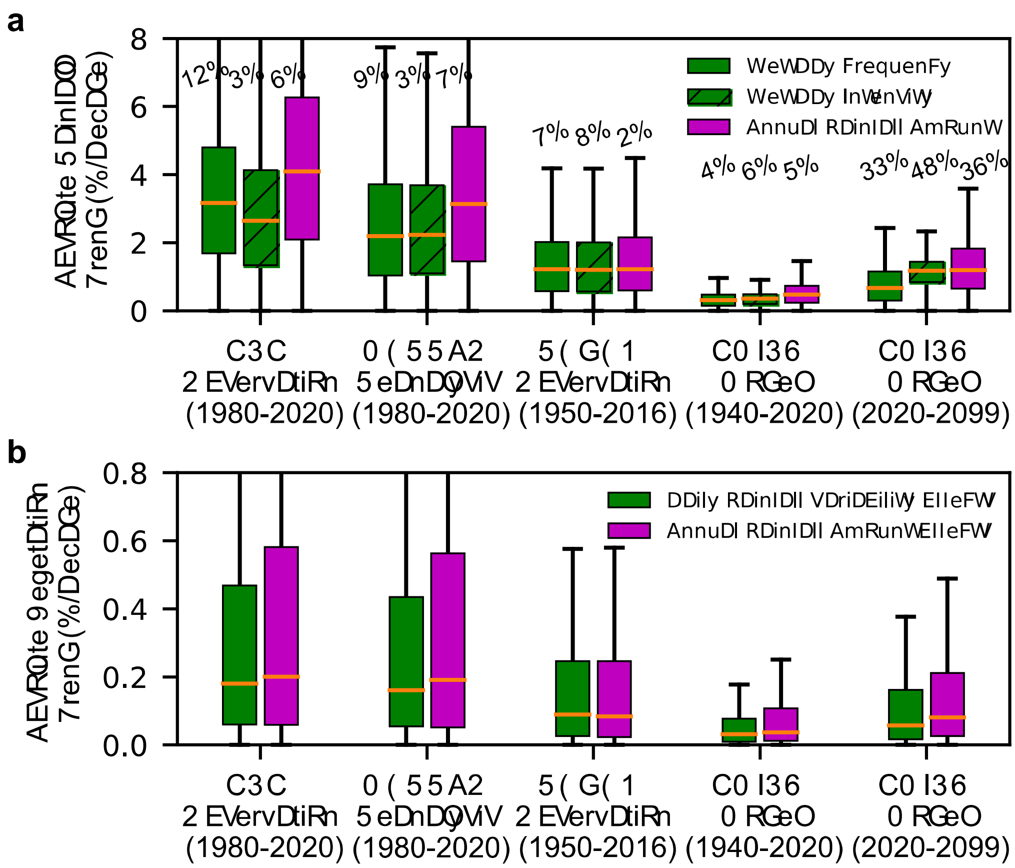

Fig. 4. | Daily rainfall variability trends are of similar absolute magnitude and spatial extent as shifts due to annual rainfall total, which consequently shifts annual mean vegetation function. (a) Absolute magnitude of trends in rainfall characteristics. Percentage of land area with significant trends are shown in text ($p<0.05$). All distributions have medians that are significantly different based on Mann-Whitney U tests ($p<0.05$). Trends over a consistent 1980-2020 period are shown in Fig. S16. Projected rainfall trends for each individual CMIP6 model are shown in Fig. S17. (b) Same as (a) but empirically estimated absolute magnitude of significant vegetation trends due to rainfall trends. Maps of empirically estimated global vegetation index trends due to changes in daily rainfall variability are shown in Extended Data Fig. 5.

Methods

Datasets

We use four retrieved vegetation indices from four different satellites. These include the Moderate Resolution Imaging Spectroradiometer (MODIS) Terra normalized difference vegetation index (NDVI) over 2003-2022 from MOD13C1 v061 at 0.05 degrees[55], the Advanced Very High Resolution Radiometer (AVHRR) NDVI over 2003-2013 from AVH13C1 version 5 at 0.1 degrees[56], the Orbiting Carbon Observatory 2 (OCO-2) solar induced fluorescence (SIF) level 2 version 11 product at a 1.3 x 2.25 km resolution over 2015-2022[57], and Global Ozone Monitoring Experiment-2 (GOME-2) SIF level 2 version 2.6.2 from MetOp-A at a 25km resolution over 2007-2017[58], which in this version is less sensitive to identified effects of sensor degradation. All datasets are linearly resampled to a 1x1 degree resolution and averaged to annual means.

The primary rainfall dataset used in the analysis is GPM IMERG V7 final run precipitation from 2003-2022 at 0.1x0.1 degrees at the daily timescale[59]. While based on satellite observations, IMERG is also bias corrected with rain gauge measurements. We additionally use Climate Prediction Center (CPC) rainfall data[60] from 1980-2020 as an alternative dataset used in place of GPM for our evaluation of vegetation sensitivity to daily rainfall variability. To evaluate observation-based trends of annual rainfall total and daily rainfall variability, we use this CPC dataset between 1980 and 2020 which aggregates both rain gauge and satellite based precipitation estimates, though with variable spatial coverage of the raw observation data and varying temporal coverages. Rainfall estimates on a gridded network (REGEN) was also obtained from the FROGS database which merges in-situ rainfall network measurements between 1950-2016[61,62]. We also use MERRA2, a model reanalysis rainfall product, between 1980 and 2020, which uses similar observed data as CPC but within a data assimilation ("PRECTOTCORR")[63]. For modeled rainfall from past to present, historical CMIP6 model trends are used across 23 models which combine historical simulations between 1940 to 2014 and projections from shared socioeconomic pathway (SSP) 245 for 2015 to 2020 similarly to previous work[52] (Table S2). Finally, considering rainfall trend projections, CMIP6 models under RCP4.5 and RCP8.5 scenarios with daily precipitation outputs are used between 2020-2099 (Table S2)[64,65]. CMIP6 datasets were linearly resampled to a 2x2 degree resolution. We use FLUXSAT gross primary production (GPP) to linearly rescale the empirical vegetation trend estimates to CO_2 flux units[66].

Other variables are used to control for additional environmental factors or provide additional evidence of main results. Lower troposphere (850mb) humidity and vapor pressure deficit are obtained from NASA's Atmospheric Infrared Sounder (AIRS) version 7 at 1x1 degrees between 2003-2022. Surface downwelling solar radiation is obtained from the Clouds and the Earth's Radiant Energy System (CERES) dataset edition 4.1 (SYN1 deg level 3 "adj_atmos_sw_down_all_surface_daily" variable) based on MODIS Aqua and Terra instruments at a one degree resolution from 2003-2022[67]. MERRA2 surface downwelling solar radiation was also used, but as an auxiliary test[68]. Land surface temperature is obtained at 1:30pm local time from the MODIS Aqua instrument MYD11C2 product v006 at 0.05 degrees from 2003-2022[69]. SMAP soil moisture level 3 enhanced product v5 was obtained between 2016 and 2022[70]. All datasets are resampled to a 1x1 degree resolution and averaged to annual means.

Mechanistic drivers used in the study include clay fraction, which is based on the harmonized world soil database[71], and maximum rooting depth obtained from a global model estimate that is validated with observations[72]. Other metrics include soil moisture thresholds for water uptake and plant response sensitivity to wet days determined from SMAP multi-temporal dual channel algorithm (MT-DCA) soil moisture and vegetation optical depth (VOD) version 5 at a 1-3 day timescale[73]. We also use International Geosphere Biosphere Programme (IGBP) land cover classifications to evaluate results in terms of different vegetation types[74].

Partial Least Squares Regression: Main Analysis

To isolate the vegetation sensitivity to daily rainfall variability, we use the following multiple linear regression:

$$Veg_t = \beta_0 + \beta_P P_t + \beta_{Frq} Frq_t + \beta_{Rs} Rs_t + \beta_{LST} LST_t + \beta_q q_t + \varepsilon \qquad (1)$$

where Veg represents the satellite-based vegetation indices, P is annual rainfall total (rainfall amount summed over a year) from GPM, Frq is wet day frequency which captures daily rainfall variability and is computed as the number of annual wet days from GPM, Rs is mean surface downwelling solar radiation over a year from MERRA2, LST is mean land surface temperature over a year from MODIS, and q is mean lower tropospheric humidity (at 850mb) over a year from AIRS. Each variable is at an annual timescale and t subscript denotes the year. β_0 is the y-intercept while the other β's are partial sensitivities of the vegetation index to the given variable. ε are the residuals. All variables are converted to z-scores by subtracting by their mean and dividing by their time series standard deviation allowing the magnitude of each β to be directly compared. This analysis is repeated setting Veg as MODIS NDVI (2003-2022), AVHRR NDVI (2003-2013), GOME-2 SIF (2007-2017), and OCO-2 SIF (2016-2022). All regressors conform to these time ranges. Note that conversion to z-score does not influence the β magnitude-dependent results in Fig. 1 because the results are nearly identical if raw variable magnitudes are inserted into Eq. 1 and then normalized by their standard deviations in post-processing.

Wet days are defined as days with daily rain totals above 1 mm in order to evaluate rainfall events that are large enough to influence vegetation[75], to avoid false positive detection of rain events given noise in the rainfall products, and because this definition is widely used[52,76]. Results in Figure 1 are ultimately not sensitive to this wet day threshold with the qualitative findings remaining similar when using 0.25 mm and 0.5 mm thresholds (Fig. S10).

We conduct a partial least squares regression, which includes determining the optimal combination of regressors in Eq. 1. To avoid overfitting the model to the data by penalizing models with more regressors, we compute the Akaike information criterion (AIC) for each model:

$$AIC = 2k + n * \ln{(RSS/n)} \quad (2)$$

where k is the number of parameters, n is the number of data pairs, and RSS is the residual sum of squared errors or the sum of squared differences between the model estimation and data. The model with the lowest AIC is selected. Only combinations of regressors are evaluated that include both P and Frq, or neither, in order to address our research questions to partition the sensitivity of vegetation to less frequent, more intense wet days from sensitivity to annual rainfall totals. This procedure allows directly comparing the magnitudes of β_P and β_{Frq}.

For the analysis on each pixel, we spatially aggregate the annual values from the adjacent 3x3 pixels to increase the sample size by a factor of 9. This is because each variable is at an annual timescale and the time series for each pixel is 8-to-20 time steps long, which results in a low sample size to carry out the partial regression analysis with Eq. 1. The effects of spatial aggregation are also tested (see Fig. S8 and "Spatial Aggregation Tests" below).

Total variance explained (R^2) of the regressors on Veg in Eq. 1 and partial variance explained of each regressor were computed. The Gromping method[77] was used to compute the partial variance explained by computing the increase in R^2 when removing the respective regressor from each combination of regressors in the model. The increased R^2 is then averaged across models. Total R^2 are typically around 0.6, a value expected when using noisy observations mainly from satellite retrievals in the regression (Fig. S4). It was thus not deemed necessary to remove pixels due to inadequate fit of annual vegetation indices.

To evaluate sensitivities from field observations, we repeated the above procedures using FLUXNET gross primary production data representing plant uptake of carbon across 178 sites distributed mainly across North America and Europe (Table S1)[78]. Data are mainly available between 1999-2014, but extend back to 1991 in a few cases. Given that FLUXNET record lengths are often less than five years, the same partial regression procedure cannot be performed on a single site. Therefore, sites are sorted from low to high mean annual precipitation and divided into 35 bins based on percentile, resulting in bins with 5 sites within 50 mm of mean annual rainfall of each other and 36 total site-years. Results are not broadly sensitive to bin size. The analysis in Eq. 1 is repeated on the site years within each bin including using the AIC model selection approach. A Monte Carlo approach is applied where the process is repeated on each bin 1,000 times to determine a distribution of β_P and β_{Frq}.

Partial Least Squares Regression: Additional Regression Model and Model Selection Tests

We chose to use AIC instead of cross validation, a commonly used model selection technique, because cross validation relies on the assumption of independent validation and training data, while spatial and temporal autocorrelation is expected for our application[79–81]. Since our approach relies on spatial aggregation, we use AIC for our main analysis, though we also test if our results remain the same using cross validation model selection.

For our auxiliary test (Fig. S7), we use five-fold cross validation[82]. Specifically, within each pixel (and including its 3x3 nearest neighbors) and for a given combination of regressors in Eq. 1, data pair samples are randomly drawn and divided into five bins. Four of these bins are used for calibration to estimate the β values in Eq. 1. The remaining bin is used for out of sample validation to estimate the root mean square error (RMSE) between the estimated vegetation index (Veg) values from the Eq. 1 model and the observed Veg values. This procedure is completed five times with each bin serving as the validation bin once. A Monte Carlo bootstrapping procedure is employed to repeat these steps 20 times to randomly generate 100 RMSE values, which are averaged to a single RMSE value. All combinations of regressors are considered. The regression model with the lowest RMSE is considered the most optimal.

To also test the sensitivity of the results to model selection, we also report our results when prescribing, a priori, the full model (with all possible regressors in Eq. (1)) and a reduced model with only rainfall regressors (annual rainfall total and the daily rainfall variability metric). We find that Figure 1 results are similar when using the AIC model section, cross validation model selection, the prescribed full model, and the prescribed reduced model (Fig. S7). The reduced model tends to reduce the ratios shown in Fig. 1 the most, though this is likely because vegetation is overly sensitive to annual rainfall total in this model since annual mean Rs, LST, and q, which tend to be correlated with mean annual rainfall, are not explicitly included in the model.

The temporal autocorrelation was estimated for the rainfall regressors (wet day frequency, wet day intensity, dry spell length, and annual rainfall total) (Fig. S18) and the four vegetation indices (MODIS NDVI, AVHRR NDVI, OCO-2 SIF, and GOME2 SIF) (Fig. S19) using the AR(1) lag-1 autocorrelation coefficient. These magnitudes tend to be below 0.1, suggesting only minor influences of temporal autocorrelation on the model selection and regressions in Eq. 1. This is because a smaller temporal autocorrelation is expected for the annually aggregated data here than for shorter timescales and thus would have less impact on the regressions.

To evaluate result dependence on the partial regression, including assumptions of linearity, we applied a random forest regression. The partial least squares regression in Eq. 1 assumes linear relationships between vegetation and each climatic variable, which approximately holds at annual timescales but might be violated in some conditions. We used the "RandomForestRegressor" package in python with the same predictors and predicted variables as the partial least squares regression[83]. As a modification, we prescribed the selected model using AIC instead of the random forest based model selection to avoid issues related to spatial and temporal autocorrelation that make the training and validation data not independent. This step also creates consistency with the partial regression approach in each pixel. We also test the random forest regression sensitivity to the choice of regression model by also prescribing reduced and full models (Fig. S7). This machine learning approach can capture nonlinear relationships between vegetation and climate variables, but has generally less interpretable outputs and it is more challenging to diagnose its errors. Therefore, the partial linear regression is featured in the main analysis with the random forest regression results shown as supporting evidence.

Partial Least Squares Regression: Additional Rainfall Metrics

Alternative daily rainfall variability metrics are also tested by replacing Frq in the regression with wet day intensity and dry spell length. Wet day intensity is defined here as the average daily rainfall depth during wet days in a given year (acknowledging intensity commonly refers to hourly rainfall rates). The dry spell length is the mean length of consecutive dry days between wet days within a given year. These metrics all represent daily rainfall variability when included in the regression along with annual rainfall totals. In other words, all metrics will capture both frequency and intensity of wet days when annual rainfall totals are simultaneously controlled for. This is because the wet day frequency multiplied by the wet day daily intensity can approximately equal the annual rainfall total.

As an alternative daily rainfall variability metric that does not use rainfall data, we repeated the analysis using SMAP soil moisture daily variability and SMAP soil moisture annual mean in place of precipitation frequency and annual rainfall total, respectively. To compute soil moisture daily variability, we removed longer timescale monthly and seasonal variability from the soil moisture time series. Specifically, all years of SMAP data were averaged to create a mean climatology and a 30-day moving window was fit to the mean soil moisture time series. This smoothed soil moisture time series was subtracted from the raw soil moisture time series. The standard deviation was computed for each year of this anomaly time series to approximately obtain only variations on sub-monthly timescales. We refer to these estimates as daily variability acknowledging some weekly and monthly variability will be integrated. Due to the SMAP record availability only beyond April 2015, the soil moisture variance analysis was only applied with MODIS NDVI and OCO-2 SIF as the predicted vegetation indices from 2016 to 2022. Ultimately, changes in sub-weekly soil moisture variability between years might not directly capture, for example, a change to less frequent, more intense wet days, and thus mainly challenges interpretation of the sign of these results (Fig. S13).

These daily rainfall variability metrics will appropriately capture some variability in atmospheric conditions that occur along with changing length of dry spells that might not be represented in an altered annual mean Rs, LST, or q. In other words, daily rainfall variability represents both sensitivity to the rain event as well as to the dry spells. To test the sensitivity of the analysis to the sub-seasonal variability of other factors, the sub-seasonal standard deviation of Rs, LST, and q are computed for each year, using the same approach for estimating the sub-seasonal variability of soil moisture. These three variability metrics are included in the regression in Eq. 1, where only the full model is considered without model selection to evaluate partitioning of sensitivities between all variables considering each variable's annual mean and sub-seasonal variability. Across the globe, vegetation is sensitive to these other sub-seasonal variability factors, but has the highest sensitivity to daily rainfall variability (Fig. S2). Furthermore, a former causal-regression analysis showed that vegetation water stress during post storm drying arises primarily from soil moisture drying and secondarily from temperature, atmospheric dryness, and incoming radiation increases[36]. Given these points and that daily rainfall variability shows some relation to these other factors (especially Rs variability; Fig. S1), we only consider daily rainfall variability in the regressions in our main analysis such that it acts as an aggregated parameter that effectively includes Rs, LST, and q variability.

Partial Least Squares Regression: Spatial Aggregation Tests

Given spatial autocorrelation in the variables used in the regression[80], it is necessary to test the effects of our 3x3 pixel window spatial aggregation, which we do here using three different tests. First, we repeated the analysis only on individual pixels without spatial aggregation to only consider temporal variability. A model selection technique was not used and the full and reduced models were prescribed a priori. This test was attempted only for MODIS NDVI (20 years; 2003-2022), AVHRR NDVI (11 years; 2003-

2013), and GOME2 SIF (11 years; 2007-2017). The sample size reduces significantly because only 20, 11, and 11 data points, respectively, are evaluated on the multiple regressions with several regressors (these sample sizes increase by a factor of 9 when using 3x3 pixel aggregation). Second, we repeated the analysis by using a 5x5 pixel aggregation and applying the regression to only the first three years of data of the four satellite datasets, which evaluates how mainly the spatial relationships between the variables contribute to the results. Finally, we evaluated the results when weighting the neighboring pixels less than the central pixel. Specifically, a geographically weighted regression (GWR) was used[84] which is a weighted linear regression that considers the center pixel as most impactful for the regression with a full 100% weight and the neighboring eight pixels as either 25% or 50% of the weight of the center pixel. In all cases, the ratios were close to those reported in Figure 1c based on the 3x3 pixel aggregation (Fig. S8). As such, we deem the results minimally sensitive to the spatial aggregation technique and remain with the 3x3 pixel aggregation in our main results. We have chosen to remain with the 3x3 spatial aggregation given that it produces similar results as the auxiliary tests and also sufficiently increases the sample size for our analysis. We chose to not show GWR in the main analysis given that it requires assumptions of different weights in the surrounding pixels, while producing similar results as the 3x3 pixel window aggregation technique.

Partial Least Squares Regression: Uncertainty Tests

To determine the variability of the vegetation sensitivity to daily rainfall variability (β_{Frq}) and its ratio to sensitivity to annual rainfall total (β_P), a bootstrapping procedure was employed in each pixel. For a given pixel and using the AIC selected model, a bootstrapping procedure is used where the regression pairs are randomly sampled with replacement and the regression coefficients are computed using these resampled pairs with Eq. 1. This procedure is repeated 5,000 times and the ratio of coefficients for the daily rainfall variability metric to that of the annual rainfall total (β_{Frq}/β_P) are computed. The 2.5th, 25th, 50th, 75th, and 97.5th percentile of the ratios are saved and their distributions across space are shown (Fig. S9).

Additionally, to compare these ratios to that produced entirely by white noise, the daily rainfall variability metric is replaced by a randomly generated standard normal time series. The regression is run with this daily rainfall variability metric being white noise while all other variables are held the same for each pixel. The rate of significance and magnitude of β_{Frq} due to random noise are computed and compared against that computed with the raw data and bootstrapping procedure.

Considering MODIS NDVI and only significant sensitivities ($p<0.05$), the 25th, 50th, and 75th percentile of the β_{Frq}/β_P ratios (spatial medians across the globe) are 0.77, 0.96, 1.19, respectively. Of the few significant ($p<0.05$) cases of the random noise test (2-4% of cases), this ratio is 0.49. When considering all data (any p-value), the 25th, 50th, and 75th percentile of the β_{Frq}/β_P ratios (spatial medians across the globe) are 0.61, 0.84, 1.14, respectively, while it is 0.15 for random noise. As such, the ratios determined in our analysis have magnitudes substantially greater than those due to noise.

Partial Least Squares Regression: Impact of Phenology

Phenology results in only parts of the year with substantial vegetation function, which can confound averaging function over the year. While the main analysis is with respect to vegetation indices averaged over the full year, we also repeat the partial regressions by evaluating growing season averages to evaluate the robustness of results to differences in vegetation function over the full year and only the growing season. Several growing season definitions were tested. Our first definition, "Growing Season Method 1", is times of year when the NDVI mean climatology is above its median, which is held constant across years. Specifically, the MODIS NDVI climatology was computed by averaging across all years between 2003-2022 into a mean seasonal cycle. This seasonal cycle was smoothed using a moving average window of 90 days. Our second definition, "Growing Season Method 2a", is based on estimating the start and end of the growing season similar to previous studies[85]. Specifically, the start and end of season are defined as the day when NDVI increases above and decreases below, respectively, the NDVI minimum plus 30% of its seasonal amplitude. The start and end of the growing season are allowed to change each year. In "Growing Season Method 2b," this same Growing Season Method 2a is repeated but with the same definition across all years. In all growing season analyses, the daily rainfall variability metrics are insensitive to the growing season length given that the rainfall total regressor is the seasonal total rainfall (which is sensitive to the growing season length) while the daily rainfall variability metrics are all normalized by the length of the growing season. We reported Growing Season Method 1 in Fig. 1 because it considers multiple growing seasons, though the other methods show similar results (Fig. S11).

The fact that the growing season analysis produces similar patterns as the presented annual mean analysis suggests phenology and changing interactions between seasons do not confound our findings. Some effects of non-linearity are also removed when considering only the growing season, thus further supporting our assumptions of linear interactions in the partial regression approach. We nevertheless choose to primarily report the annual mean results in the main text because daily rainfall variability includes effects both during rain events and during dry spells, the latter of which can influence vegetation outside of a growing season. Furthermore, growing season definitions vary and are inconsistent across the literature and thus our several definitions are provided as auxiliary analyses for reference.

Partial Least Squares Regression: Multi-collinearity and Causality

Several other limitations and confounding effects were addressed. First, multi-collinearity, or correlation between regressors that inflates the variance of their β estimates, are partly reduced by use of the partial regression technique to select the model with the optimal regressors[86]. However, annual rainfall total and wet day rainfall frequency are correlated, but are still kept together within the regression in order to address our research questions about their partitioned relation with vegetation function. Variance inflation factors (VIF) were therefore assessed between annual rainfall total (P) and wet day frequency (Frq) in each pixel to determine whether P and Frq have multi-collinearity that greatly increases the variances of β_P and β_{Frq}. VIF is generally less than 5 meaning that it is acceptable to include both P and Frq in the regression (Extended Data Fig. S3). In the case when mean annual precipitation is below 400 mm/year, the VIF increases to between 5 and 10. However, VIF is below 5 when using wet day intensity in place of wet day frequency in this lower rainfall bin and results are ultimately qualitatively the same when using intensity in place of frequency. As such, multi-collinearity is not expected to be substantially influencing results here. Including wet day intensity as an additional regressor to P and Frq in Eq. 1 creates an overdetermined problem and results in very high VIF (>>10). Therefore, only wet day frequency is used as a regressor along with P. However, to gain confidence in results, the analysis is repeated using wet day intensity and dry spell length (mean number of dry days between wet days) each in place of wet day frequency as validation of wet day frequency results.

Our analysis does not directly consider effects of different types of wet day timing patterns (e.g. concentrated in certain periods of spread out uniformly across the year), since these timing effects were found to be secondary in importance to wet day frequency and intensity at a field scale analysis[87].

Another key limitation is that the regression-based relationships do not indicate causality. The direction of causality is presumably that the daily rainfall variability is impacting vegetation, with feedback effects in the opposite direction of vegetation on the atmosphere likely smaller[88]. However, the regressions do not allow us to make a stronger argument that daily rainfall variability is causing the vegetation function responses. Nevertheless, the partial regressions are sufficient for addressing our questions of vegetation sensitivity to daily rainfall variability compared to other factors. Much of the understanding of vegetation relation to climate variables comes from such regression and non-causal relationship analyses[24,25,89].

Analysis of Vegetation Sensitivity to Wet Day Frequency and Intensity

The global spatial distribution of absolute values β_P and β_{Frq} and their explained variances were compared. For the satellite data, we computed an ensemble average β_P and β_{Frq} in each pixel across the four satellites. For the partial regression analysis on both satellite and field data, the ratio between β_{Frq} and β_P was computed. For the random forest regression on satellite data, the SHAP values (Shapley Additive Explanation) were computed to interpret the random forest outputs using the SHAP package in python[90]. The mean absolute SHAP values have a similar interpretation as normalized β_{Frq} and β_P do, specifically the relative magnitude of sensitivity of a vegetation index to a given predictor variable. When averaging across the metrics across the four satellites, it is assumed here that the vegetation sensitivity to the environmental factors are constant between 2003-2022, given the dataset ranges occupy different years in this range. Therefore, this allows the effects from different ranges of satellite records to be averaged.

Consistency in the spatial pattern of the sign and statistical significance of β_{Frq} sensitivity across the four vegetation datasets provides another form of confidence in the results. A such, we define a “degree of agreement” metric to be evaluated in each pixel as the count of satellite-based vegetation datasets with positive, significant β_{Frq} minus the count of satellite-based vegetation datasets with negative, significant β_{Frq}. Only pixels with an absolute value Degree of Agreement of greater than or equal to 2 are considered statistically significant when considering the ensembles across the four datasets. Higher absolute values result from several of the four satellite datasets agreeing in statistical significance ($p<0.05$) and sign of sensitivity. Positive Degree of Agreement values indicate positive relationships of wet day frequency with annual vegetation indices across most of the datasets. When β_{Frq} show no statistically significance or they have opposing signs across the four satellites, the Degree of Agreement approaches zero.

The percentage of global pixels with statistically significant vegetation sensitivities to wet day frequency and intensity as well as annual rainfall total were also computed. These areal percentages are based on ensemble mean β_P and β_{Frq} across the four satellite-based vegetation indices that are statistically significant based on the degree of agreement. Only pixels were considered that are dominantly vegetated (non-bare soil based on IGBP classification), below 60 degrees latitude, non-mountainous (based on IGBP classification), and have at least 20 annual data points used in their regression. Screening mountainous regions partially removes pixels with snowmelt, though we acknowledge that snowmelt and runoff will influence non-mountainous adjacent pixels.

Mechanistic Analysis

Given the differing signs of vegetation sensitivity to wet day frequency and intensity, we also evaluated the percentage of pixels with statistically significant positive and negative vegetation sensitivities to less frequent, more intense wet days. We evaluated these relations across a mean annual precipitation gradient where the bins are partitioned such that there are the same number of global pixels in each of the five bins (approximately 800). We also compute the same percentages across pixels with the same IGBP classes to evaluate effects of vegetation type.

We evaluate which observable mechanistic drivers explain the spatial gradient of vegetation sensitivities to less frequent, more intense wet days. We specifically chose variables that would directly modulate how plants respond to a more intense rain event and/or longer dry spell as well as are observed or estimated at global scales. The potential drivers we evaluate include clay fraction (soil texture), plant response sensitivity to wet days, soil moisture mean relative to its soil moisture thresholds for plant water uptake, maximum rooting depth, and the sensitivity of mean annual soil moisture, surface downwelling solar radiation, and VPD to less frequent, more intense wet days.

Plant response sensitivity to wet days and soil moisture thresholds for plant water uptake are determined in the same manner as from previous work[37]. In summary, SMAP soil moisture at 9km is used to identify interstorm periods when the soil is drying, defined as at least three consecutive SMAP satellite overpasses of decreasing soil moisture. It was previously found that VOD tends to increase at higher soil moisture and decrease at lower soil moisture values during drydowns[37]. As such, the soil moisture value for which VOD on average begins decreasing during drydowns is the estimated soil moisture threshold. The plant response sensitivity to wet days is the median dVOD/dt rate of change above the soil moisture threshold. To decouple relations to determined soil moisture threshold and to plant response sensitivities to wet days, in the determination of plant response sensitivities to wet days, the soil moisture threshold is set as the median soil moisture for each pixel. The plant response sensitivities to wet days are normalized by the mean VOD over the 2015-2020 time series to create a fractional rate of VOD increase over an interstorm. These metrics are determined from all drydowns at 9km pixels, but are aggregated to a one degree resolution for consistency with the analysis in this paper. See ref. [37] for more details.

The soil moisture mean relative to the soil moisture threshold is computed by subtracting the soil moisture threshold from the mean soil moisture. This relative mean soil moisture is deemed more related to effects of daily rainfall variability (than annual rainfall total or mean soil moisture) because it assesses the degree to which rainfall pulses and dry spells are generally occurring under plant water stress conditions for that location. Evaluating mean soil moisture by itself would otherwise not provide information on whether plants are stressed.

The relationship of wet day frequency with mean annual soil moisture, mean annual surface downwelling solar radiation, and mean annual VPD are determined by:

$$Y = \beta_0 + \gamma_P P + \gamma_Y Frq + \varepsilon \qquad (3)$$

where Y is mean annual SMAP soil moisture, mean annual CERES surface downwelling solar radiation, or mean annual AIRS vapor pressure deficit. γ_Y is the sensitivity of the respective climatic variable to wet day frequency, analogously to β_{Frq}, as partitioned from sensitivities to annual rainfall total. The analysis is repeated similarly to that of Eq. 1. With less frequent, more intense wet days, annual mean VPD is higher (79% pixels positive, 2% pixels negative), annual mean surface downwelling solar radiation is higher (64% pixels positive, 9% pixels negative), and annual mean soil moisture tends to be lower (12% pixels positive, 24% pixels negative) (Fig. S15).

We aim to determine the degree to which the spatial rainfall gradient of the ensemble mean β_{Frq} is sensitive to each factor and why β_{Frq} tends to switch in sign with increasing annual rainfall totals (Fig. 3). Thus, β_{Frq} and each mechanistic factor is binned into 50 equally sized mean annual precipitation bins and the median of each variable is computed. Conditioning on these bins in this way allows for controlling for the mean annual precipitation gradient, or effectively conditioning on the rainfall gradient. Each variable is converted to its z-score by subtracting by its bin average and dividing by its binned standard deviation. The following is then computed:

$$\beta_{Frq} = \beta_0 + \beta_{Clay} Clay + \beta_{Pulse} Pulse + \beta_{RootDepth} RootDepth + \beta_{Threshold} Threshold + \beta_{VPD}\gamma_{VPD} + \beta_{SM}\gamma_{SM} + \beta_{Rs}\gamma_{Rs} + \varepsilon \qquad (4)$$

The analysis therefore estimates which climate variables explain the annual rainfall total driven gradient of β_{Frq}. Uncertainty bounds and statistical significance are determined via bootstrapping by randomly sampling with replacement pixels across the globe and repeating the analysis in a Monte Carlo format with 200 iterations. Statistical significance is determined if the β of the explanatory variable has the same sign for its 2.5th and 97.5th percentiles. The main analysis was performed on the β_{Frq} ensemble mean across MODIS NDVI, AVHRR NDVI, OCO-2 SIF, and GOME-2 SIF. However, there is little variability of results when performing the analysis on each individual satellite vegetation index. We also obtain the same results when performing the regression on the β_{Frq} spatial area of significant sensitivities ($p<0.05$).

Trend Analysis

Temporal trends in annual rainfall total, wet day frequency, and wet day intensity are computed by regressing the z-score anomalies of these annual-scale properties across the years of their time series in each pixel. For historical trends from 1980 to 2020, we use CPC observation-based rainfall, to account for complex climate changes features that might create uncertainty in models[91], and MERRA2 model reanalysis rainfall. We also evaluate historical CMIP6 model-based precipitation from 23 models, but the 1940-2020 period was chosen for CMIP6 historical trends to be of consistent time length as the CMIP6 projections and reduce effects of internal and decadal variability. As an additional observation-based dataset, we evaluate trends in spatially gridded rain gauge data from the REGEN dataset between 1950-2016. For projections, these properties are computed using CMIP6 models with daily outputs over 2020-2099. This includes 27 models for RCP8.5 (Table S2). Note that we also evaluate trends alternatively with RCP4.5 and find that the trend magnitude and spatial extent is reduced (not shown). However, our same conclusions in Figure 4 hold about relative extent and magnitude of daily rainfall variability. The CPC and MERRA2 datasets were rescaled to one-degree grids using linear resampling. Since most CMIP6 model resolutions are lower than one degree resolution, CMIP6 models were rescaled to two-degree grids.

Temporal autocorrelation can artificially induce trends in a time series[92,93]. To remove temporal autocorrelation from the time series of annual rainfall total for each dataset, the autoregressive lag-1 (AR(1)) coefficient is removed by computing $P_t – r_{t-1}P_{t-1}$, where r_{t-1} is the AR(1) coefficient or correlation between P_t and P_{t-1}. Next, in each pixel, statistical significance is determined through Mann-Kendall trend tests of whether the trend magnitudes are different from zero ($p<0.05$). Then, following a nearly identical procedure to previous work[92–95], multiple hypothesis testing is applied to further remove false positive trend detections given that false positives will occur in isolated cases with inherent spatial autocorrelation in the dataset creating a cluster of false positives[95]. The test thus finds a threshold for spatial cluster size of significant trends, below which the cluster is likely formed by false positive rainfall trends. To compute this critical cluster size, a joint permutation is applied where the time series in each pixel are randomly re-ordered without replacement and a trend is computed along with a Mann-Kendall trend test for each pixel. This same random permutation is applied throughout all global pixels to conserve the spatial autocorrelation structure of the data and determine false positive cluster sizes. Clusters of these false positives are counted considering first order (queen) neighbors. The largest cluster size is recorded based on this randomized time series ordering. This process is repeated 1,000 times for each dataset and the 95th percentile of maximum cluster size is the determined threshold. For a given dataset, it was determined that after approximately 500 iterations, the maximum cluster size and consequently the percent area of significant trends tended to converge to the same value. Finally, the cluster sizes are determined for the trend computation on the raw data (1980-2020 or 2020-2099) and clusters of statistically significant trends smaller than this cluster threshold are considered not statistically significant and likely due to false positive trends. Note that this process is carried out for each of the CMIP6 models individually.

We evaluate trends across several rainfall datasets not as a comparison of trends, but rather to determine whether our main arguments about relative differences in daily rainfall variability and annual rainfall total trends hold under limitations presented by each dataset (see SI text for discussion of limitations). We note that the datasets between the 1980-2020 periods all show the same overarching results about the trend magnitude and spatial area of significant trends ($p<0.05$) when comparing trends of daily rainfall variability and trends of total annual rainfall (Figs. S16, S20). For REGEN and CMIP6 historical record, when shortening the time series to only after 1980, the spatial extent of significant trends is reduced, but the same conclusion remains of the similarity of magnitude and spatial extent of trends is similar between daily rainfall variability and total annual rainfall.

To empirically estimate vegetation function trends, these aforementioned rainfall trends are multiplied by the partitioned vegetation sensitivities to these rainfall features (β_P and β_{Frq}), which are mean sensitivities from the different satellites. These trend estimates are uncertain because they assume that vegetation sensitivity to the rainfall metrics are constant in time, which would not hold under CO_2 fertilization[96]. Nevertheless, we expect that the regressions would partition the sensitivity of the vegetation index due to daily rainfall variability and would only have minor biases due to the likely smaller influences of CO_2 fertilization. These vegetation sensitivities are computed using 20-year and less time periods which are influenced by sub-decadal variability like El Nino Southern Oscillation (ENSO). Since atmospheric CO_2 has increased monotonically, we expect less of an impact on interannual variability of the vegetation indices, which we show is strongly driven by year-to-year changes in annual rainfall and daily rainfall variability among other factors. The estimated trends are rescaled to obtain a percent change per year using FLUXSAT GPP units[66]. The vegetation trend is in standard normalized format ($GPP-E[GPP])/\sigma[GPP]$). To approximate percent change units, the vegetation trend is multiplied by GPP interannual mean standard deviation then divided by GPP mean. Therefore, the units are in mean percent change of GPP per year (or ($GPP-E[GPP])/E[GPP]$).

Methods References

55. Didan, K. MODIS/Terra Vegetation Indices 16-Day L3 Global 0.05 Deg CMG V061. 2021, distributed by NASA EOSDIS Land Processes DAAC, https://doi.org/10.5067/MODIS/MOD13C1.061. (2021).
56. Vermote, E. *et al.* NOAA CDR Program. (2014): NOAA Climate Data Record (CDR) of Normalized Difference Vegetation Index (NDVI), Version 4. AVH13C1. NOAA National Centers for Environmental Information. https://doi.org/10.7289/V5PZ56R6. Accessed 01/15/2023. (2014).
57. OCO-2-Science-Team, Gunson, M. & Eldering, A. OCO-2 Level 2 bias-corrected solar-induced fluorescence and other select fields from the IMAP-DOAS algorithm aggregated as daily files, Retrospective processing V10r, Greenbelt, MD, USA, Goddard Earth Sciences Data and Information Services Center (GES DIS. (2020).
58. Joiner, J. *et al.* Global monitoring of terrestrial chlorophyll fluorescence from moderate-spectral-resolution near-infrared satellite measurements: methodology, simulations, and application to GOME-2. *Atmos. Meas. Tech.* **6**, 2803–2823 (2013).
59. Huffman, G. ., Stocker, E. F., Bolvin, D. T., Nelkin, E. J. & Tan, J. GPM IMERG Final Precipitation L3 Half Hourly 0.1 degree x 0.1 degree V06, Greenbelt, MD, Goddard Earth Sciences Data and Information Services Center (GES DISC), Accessed: [03.01.20. (2019).
60. Xie, P. *et al.* A gauge-based analysis of daily precipitation over East Asia. *J. Hydrometeorol.* **8**, 607–626 (2007).
61. Contractor, S. *et al.* Rainfall Estimates on a Gridded Network (REGEN) - A global land-based gridded dataset of daily precipitation from 1950 to 2016. *Hydrol. Earth Syst. Sci.* **24**, 919–943 (2020).
62. Roca, R. *et al.* FROGS: A daily 1° × 1° gridded precipitation database of rain gauge, satellite and reanalysis products. *Earth Syst. Sci. Data* **11**, 1017–1035 (2019).
63. Reichle, R. H. *et al.* Land Surface Precipitation in MERRA-2. *J. Clim.* **30**, 1643–1664 (2017).
64. Eyring, V. *et al.* Overview of the Coupled Model Intercomparison Project Phase 6 (CMIP6) experimental design and organization. *Geosci. Model Dev.* **9**, 1937–1958 (2016).
65. Copernicus Climate Change Service Climate Data Store. CMIP6 climate projections. Copernicus Climate Change Service (C3S) Climate Data Store (CDS). DOI: 10.24381/cds.c866074c (Accessed on 15-04-2023). (2021).
66. Joiner, J. *et al.* Estimation of terrestrial global gross primary production (GPP) with satellite data-driven models and eddy covariance flux data. *Remote Sens.* **10**, 1–38 (2018).
67. NASA/LARC/SD/ASDC. CERES and GEO-Enhanced TOA, Within-Atmosphere and Surface Fluxes, Clouds and Aerosols Daily Terra-Aqua Edition4A [Data set]. NASA Langley Atmospheric Science Data Center DAAC. Retrieved from https://doi.org/10.5067/Terra+Aqua/CERES/SYN1degDay_L3.004A. (2017).
68. Gelaro, R. *et al.* The modern-era retrospective analysis for research and applications, version 2 (MERRA-2). *J. Clim.* **30**, 5419–5454 (2017).
69. Wan, Z., Hook, S. & Hulley., G. MYD11C2 MODIS/Aqua Land Surface Temperature/Emissivity 8-Day L3 Global 0.05 Deg CMG V006. 2015, distributed

by NASA EOSDIS Land Processes DAAC, https://doi.org/10.5067/MODIS/MYD11C2.006. (2015).
70. O'Neill, P. E., S. Chan, E. G. Njoku, T. Jackson, R. Bindlish, and J. Chaubell. (2019). SMAP Enhanced L3 Radiometer Global Daily 9 km EASE-Grid Soil Moisture, Version 3 [Data Set]. Boulder, Colorado USA. NASA National Snow and Ice Data Center Distributed .
71. O'Neill, P. Soil Moisture Active Passive (SMAP) Algorithm Theoretical Basis Document (ATBD) SMAP Level 2 & 3 Soil Moisture (Passive). 1–75 (2012).
72. Fan, Y., Miguez-Macho, G., Jobbágy, E. G., Jackson, R. B. & Otero-Casal, C. Hydrologic regulation of plant rooting depth. *Proc. Natl. Acad. Sci. U. S. A.* **114**, 10572–10577 (2017).
73. Feldman, A. F., Konings, A., Piles, M. & Entekhabi, D. The Multi-Temporal Dual Channel Algorithm (MT-DCA) (Version 5) [Data set]. *Zenodo* (2021). doi:https://doi.org/10.5281/zenodo.5619583
74. Kim, S. Ancillary Data Report: Landcover Classification. *Jet Propuls. Lab. Calif. Inst. Technol., JPL* D-53057. (2013).
75. Sala., O. E. & Lauenroth, W. K. Small Rainfall Events: An Ecological Role in Semiarid Regions. *Oecologia* **53**, 301–304 (1982).
76. Giorgi, F., Raffaele, F. & Coppola, E. The response of precipitation characteristics to global warming from climate projections. *Earth Syst. Dyn.* **10**, 73–89 (2019).
77. Grömping, U. Estimators of relative importance in linear regression based on variance decomposition. *Am. Stat.* **61**, 139–147 (2007).
78. Pastorello, G., Trotta, C., Canfora, E. & Authors), (284 more. The FLUXNET2015 dataset and the ONEFlux processing pipeline for eddy covariance data. *Sci. Data* **7**, 225 (2020).
79. Ploton, P. *et al.* Spatial validation reveals poor predictive performance of large-scale ecological mapping models. *Nat. Commun.* **11**, 1–11 (2020).
80. Lewińska, K. E. *et al.* Beyond "greening" and "browning": Trends in grassland ground cover fractions across Eurasia that account for spatial and temporal autocorrelation. *Glob. Chang. Biol.* **29**, 4620–4637 (2023).
81. Ludwig, M., Moreno-Martinez, A., Hölzel, N., Pebesma, E. & Meyer, H. Assessing and improving the transferability of current global spatial prediction models. *Glob. Ecol. Biogeogr.* **32**, 356–368 (2023).
82. James, G., Witten, D., Hastie, T. & Tibshirani, and R. *An Introduction to Statistical Learning: With Applications in R.* (Springer, 2014).
83. Pedregosa, F. *et al.* Scikit-learn: Machine Learning in Python. *J. Mach. Learn. Res.* **12**, 2825–2830 (2011).
84. Brunsdon, C., Fotheringham, A. S. & Charlton, M. E. Geographically weighted regression: a method for exploring spatial nonstationarity. *Geogr. Anal.* **28**, 281–298 (1996).
85. Li, Y. *et al.* Widespread spring phenology effects on drought recovery of Northern Hemisphere ecosystems. *Nat. Clim. Chang.* **13**, 182–188 (2023).
86. Greene, W. H. *Econometric Analysis*. (Prentice Hall, 2003).
87. Griffin-Nolan, R. J., Slette, I. J. & Knapp, A. K. Deconstructing precipitation variability: Rainfall event size and timing uniquely alter ecosystem dynamics. *J. Ecol.* 1–14 (2021). doi:10.1080/10643389.2012.728825

88. Green, J. K. *et al.* Regionally strong feedbacks between the atmosphere and terrestrial biosphere. *Nat. Geosci.* **10**, 410–414 (2017).
89. Madani, N., Kimball, J. S., Jones, L. A., Parazoo, N. C. & Guan, K. Global analysis of bioclimatic controls on ecosystem productivity using satellite observations of solar-induced chlorophyll fluorescence. *Remote Sens.* **9**, 530 (2017).
90. Lundberg, S. M. & Lee, S.-I. A Unified Approach to Interpreting Model Predictions. in *31st Conference on Neural Information Processing System* (2017).
91. Andrews, T. *et al.* On the Effect of Historical SST Patterns on Radiative Feedback. *J. Geophys. Res. Atmos.* **127**, (2022).
92. Bueso, D. *et al.* Soil and vegetation water content identify the main terrestrial ecosystem changes. *Natl. Sci. Rev.* (2023).
93. Ives, A. R. *et al.* Statistical inference for trends in spatiotemporal data. *Remote Sens. Environ.* **266**, 112678 (2021).
94. Cortés, J. *et al.* Where Are Global Vegetation Greening and Browning Trends Significant? *Geophys. Res. Lett.* **48**, 1–9 (2021).
95. Cortés, J., Mahecha, M., Reichstein, M. & Brenning, A. Accounting for multiple testing in the analysis of spatio-temporal environmental data. *Environ. Ecol. Stat.* **27**, 293–318 (2020).
96. Keenan, T. F. *et al.* Increase in forest water-use efficiency as atmospheric carbon dioxide concentrations rise. *Nature* **499**, 324–327 (2013).

Data Availability Statement

The data used and created in the study are available in two repositories. The processed data inputs are available on Zenodo at https://zenodo.org/records/10947071. The output data and reduced-size example input data are available on Zenodo at https://zenodo.org/records/13551521. All datasets used in the study are freely available and were obtained as follows. The MODIS NDVI product can be obtained from https://modis.gsfc.nasa.gov/data/dataprod/mod13.php. AVHRR NDVI can be obtained from https://www.ncei.noaa.gov/data/land-normalized-difference-vegetation-index/access/. GOME-2 SIF can be downloaded from https://daac.ornl.gov/SIF-ESDR/guides/MetOpA_GOME2_SIF.html. OCO-2 SIF can be obtained from https://disc.gsfc.nasa.gov/datasets/OCO2_L2_Lite_SIF_10r/summary. The MT-DCA vegetation optical depth dataset retrieved from SMAP is freely available at https://doi.org/10.5281/zenodo.5579549. AIRS humidity and air temperature data are available at https://airs.jpl.nasa.gov/data/get-data/standard-data/. The MODIS land surface temperature product can obtained from https://lpdaac.usgs.gov/products/myd11c2v006/. MERRA2 precipitation data can be accessed at https://gmao.gsfc.nasa.gov/reanalysis/MERRA-2/data_access/. CERES radiation can be accessed at: https://asdc.larc.nasa.gov/project/CERES/CER_SYN1deg-Day_Terra-Aqua-MODIS_Edition4A. SMAP soil moisture can be obtained from https://nsidc.org/data/smap/data. GPM precipitation outputs are available at https://gpm.nasa.gov/data/directory. CPC precipitation data are available at https://psl.noaa.gov/data/gridded/data.cpc.globalprecip.html. REGEN precipitation data are available at https://thredds-x.ipsl.fr/thredds/catalog/FROGs/REGEN_ALL_V1-2019/catalog.html. FLUXNET gross primary production observations can be obtained from https://fluxnet.org. CMIP6 rainfall projections can be obtained from https://cds.climate.copernicus.eu.

Code Availability Statement

The code is available on a Zenodo repository at https://zenodo.org/records/13551521 to both create the figures and conduct the analysis. This repository includes the main analysis outputs and example input data. The full processed data inputs are available on another Zenodo repository at https://zenodo.org/records/10947071.

Acknowledgements

A.F.F. was supported by an appointment to the NASA Postdoctoral Program at the NASA Goddard Space Flight Center, administered by Oak Ridge Associated Universities under contract with NASA. A.F.F. was also partly supported by a NASA Terrestrial Ecology Program scoping study for dryland ecosystems. A.G.K was supported by the Alfred P. Sloan Foundation and by NSF DEB 1942133. W.K.S. and B.P. acknowledge support from the NASA Carbon Cycle Science grant no. 80NSSC23K0109. M.A. acknowledges Swiss National Science Foundation grant no. 206603. L.W. acknowledges partial support from the US National Science Foundation (DEB-2307257, DEB-2406931). USDA is an equal-opportunity employer and provider. We acknowledge the World Climate Research Programme, which, through its Working Group on Coupled Modelling, coordinated and promoted CMIP6. We thank the climate modeling groups for producing and making available their model output, the Earth System Grid Federation (ESGF) for archiving the data and providing access, and the multiple funding agencies who support CMIP6 and ESGF. This work used eddy covariance data acquired and shared by the FLUXNET community, including these networks: AmeriFlux, AfriFlux, AsiaFlux, CarboAfrica, CarboEuropeIP, CarboItaly, CarboMont, ChinaFlux, Fluxnet-Canada, GreenGrass, ICOS, KoFlux, LBA, NECC, OzFlux-TERN, TCOS-Siberia, and USCCC. The FLUXNET eddy covariance data processing and harmonization was carried out by the ICOS Ecosystem Thematic

Center, AmeriFlux Management Project and Fluxdata project of FLUXNET, with the support of CDIAC, and the OzFlux, ChinaFlux and AsiaFlux offices.

Author Contributions

A.F.F. conceived the study with input from B.P. A.F.F. conducted the analysis and wrote the initial manuscript. A.G.K., P.G., J.J., A.C., and B.P. provided guidance on the methods throughout the analysis. M.A., L.W., W.K.S., and J.A.B. provided guidance in part on methods and mainly on the interpretation of results. All authors contributed substantial revisions to the text and figures.

Competing Interests

The authors declare no competing interests

Extended Data Figure Captions

Extended Data Fig. 1. | Across historical simulations and projections, rainfall is becoming less frequent, but more intense. Historical and projected rainfall trends of (a, b) wet day frequency, and (c, d) wet day intensity, and (e, f) annual rainfall total using CMIP6 historical simulations (1940-2020) and CMIP6 RCP8.5 models (2020-2099).

Extended Data Fig. 2. | Across observation-based rainfall datasets, rainfall is becoming less frequent, but more intense. Rainfall trends of (a, b) wet day frequency, and (c, d) wet day intensity, and (e, f) annual rainfall total using CPC gridded observations (1980-2020) and MERRA2 model reanalysis (1980-2020).

Extended Data Fig. 3. | Wet day frequency and annual rainfall amount have enough uncorrelated information to be included together and partitioned in a regression. (a) Variance inflation factor of wet day frequency and intensity. Higher values (especially much over 5) indicate multi-collinearity with annual rainfall mean and thus higher uncertainty partitioning effects between the variables. (b) Interannual coefficient of variation computed as the interannual standard deviation divided by interannual mean for each respective rainfall characteristic. Similar magnitudes between variables suggest variability of one variable is not dominating the regression.

Extended Data Fig. 4. | Mechanistic explanation of vegetation sensitivity to more intense, less frequent wet days across the global mean rainfall gradient (in Fig. 3). (a) Effect of soil, plant, and atmospheric factors on vegetation sensitivity to more intense, less frequent wet days. ** indicates significance ($p<0.05$). Positive values suggest that increasing the respective driver promotes higher vegetation behavior in years with more intense, less frequent wet days. Computation of individual mechanistic factors is discussed in the Methods and their relationships with mean annual rainfall are shown in Fig. S15. Mean VPD, Soil Moisture, and Solar Radiation “Sensitivity” refers to the response of these climate variables to more intense, less frequent wet days (see text and Methods). (b) Variance explained of factors in (a).

Extended Data Fig. 5. | Empirically estimated vegetation trends due to daily rainfall variability trends. Spatial maps of empirically estimated vegetation trends due to trends in daily rainfall variability from (a) CPC, (b) MERRA2, (c) CMIP6 historical simulations, and (d) CMIP6 RCP8.5 projections.